arXiv:1702.02881v1 [astro-ph.EP] 9 Feb 2017

Texture and composition of Titan's equatorial region inferred from Cassini SAR inversion: Implications for aeolian transport at Saturn's largest moon

Antoine Lucas[a,b,*], Sébastien Rodriguez[a,b], Florentin Lemonnier[c,d], Alice Le Gall[d], Cécile Ferrari[a,b], Philippe Paillou[e], Clément Narteau[b]

[a] *AIM CEA-Saclay, Université Paris Diderot, USPC, Paris, France*
[b] *IPGP, USPC, Paris, France*
[c] *LMD,UPMC Univ. Paris 06, France*
[d] *LATMOS/IPSL, UVSQ Université Paris-Saclay, UPMC Univ. Paris 06, CNRS, Guyancourt, France*
[e] *Observatoire de Bordeaux, Université de Bordeaux, Bordeaux, France*

Abstract

Sand seas on Titan may reflect the present and past climatic conditions. Understanding the morphodynamics and physico-chemical properties of Titan's dunes is therefore essential for a better comprehension of the climatic and geological history of the largest Saturn's moon. We derived quantitatively surface properties (texture, composition) from the modelling of microwave backscattered signal and Monte-Carlo inversion of despeckled Cassini/SAR data over sand sea. We show that dunes and interdunes have significantly different physical properties. Dunes are globally more microwave absorbent than the interdunes. The interdunes present multi-scale roughness with a higher dielectric constant than the dunes. Considering the composition, the interdunes are in between the dunes and the radar bright inselbergs, suggesting the presence of a shallow layer of non-mobilized sediment in between the dunes. Additionally potential secondary bedforms, such as ripples and avalanches, may have been detected. Our findings strongly suggest that sand seas evolve under current multi-directional wind regimes. Consequently sediment inventory and climatic conditions are being re-evaluated.

*Corresponding author
Email address: dralucas@geophysx.edu.eu.org (Antoine Lucas)

Keywords: Titan, sand seas, sediment transport, climate, microwave, Bayesian inference

1. Introduction

Along with the lakes and fluvial networks, Cassini-Huygens mission discovered that large sand seas occupy Titan's equatorial regions, covering 15-20% of the global surface [Lorenz et al., 2006; Radebaugh et al., 2008; Radebaugh, 2013; Le Gall et al., 2011; Rodriguez et al., 2014; Aharonson et al., 2014].

As detected by the spectro-imager VIMS (Visual and Infrared Mapping Spectrometer) instrument onboard Cassini spacecraft [Soderblom et al., 2007; Barnes et al., 2008; Rodriguez et al., 2014] and supported by the RADAR Radiometer [Le Gall et al., 2011], these vast sand sea units constitute a major organics reservoir at the surface, and consequently have a large impact on the geological and climatic history of Titan Aharonson et al. [2014].

Thanks to the high spatial resolution of the SAR imager mode of the RADAR instrument on board Cassini [Elachi et al., 2004], individual linear dunes have been identified within those sand seas and mapped at the global scale [Lorenz et al., 2006; Radebaugh et al., 2008; Le Gall et al., 2011; Rodriguez et al., 2014] (Figure 1). Geomorphic analyses have been carried out and show that most of the bedforms are 100-to-1000's km long linear dunes with a crest-to-crest distance of about 3 km [Lorenz et al., 2006, 2010; Le Gall et al., 2011; Savage et al., 2014; Lucas et al., 2014b]. Available topographic information and/or radarclinometric assessment gives an estimation of an average height of 50-150 m approximately [Neish et al., 2010; Mastrogiuseppe et al., 2014]. In some RADAR swaths, interdune areas are clearly distinguishable from the dunes as exemplify on figure 2 showing a subset of Belet sand seas. Sources for organic sand is yet to be identified at the surface, and might have disappeared as aeolian systems are considered to be old Rodriguez et al. [2014].

All studies agree on the eastwards propagation of the linear and barchanoid dunes [Lorenz et al., 2006; Radebaugh et al., 2008; Lucas et al., 2014a]. Due to

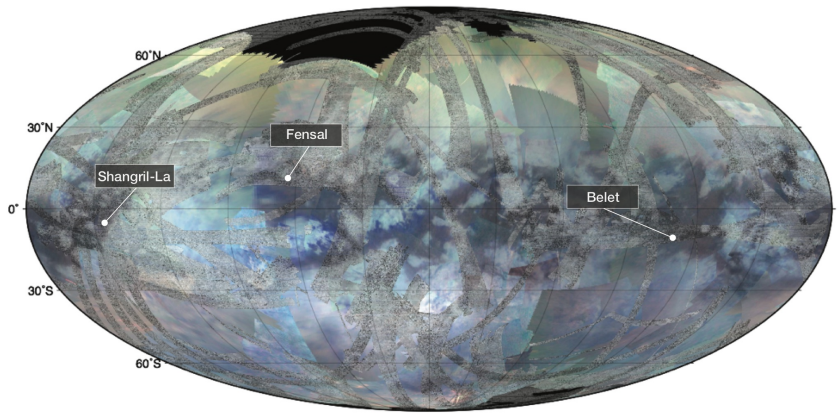

Figure 1: Titan global map centered in 0° of longitude showing regions of interest location, namely Shangri-La, Fensal and Belet sand seas. The basemap is an empirical corrected VIM's mosaik from [Rodriguez et al., 2014]. SAR swath are overlayed in transparency for sake of clarity.

our limited insights on the current climatic conditions, available GCM (Global Circulation Models) fail in generating surface winds with eastwards mean direction and sufficient strength allowing sediment transport [Lebonnois et al., 2012; Charnay et al., 2015; Tokano, 2010; Ewing et al., 2015; Lucas et al., 2014a; McDonald et al., 2016]. Surface winds on Titan are predicted to be primarily bimodal, blowing seasonally to the south-west or the north-west, with an average speed never exceeding 1 m/s near the surface. Consequently, while it is commonly admitted that these aeolian systems are mature but still active nowadays, and considering the 50, 000-year timescale for Titan's dunes to reorient to follow global climatic changes [Ewing et al., 2015], there is a long-standing debate on whether their orientations reflect past or current wind conditions at Titan's surface [Ewing et al., 2015; Lucas et al., 2014a; Charnay et al., 2015; McDonald et al., 2016]. Depending on the geomorphic interpretations, different morphodynamics have been proposed: i) reorientation of dune crests resulting from shifts in wind direction and strength and sediment availability on long-term climate cycles controlled by variations of Saturn's orbit [Ewing et al., 2015; McDonald et al., 2016]; ii) equinoctial gusts and/or storms such as those observed in 2011

[Turtle et al., 2011a], can generate winds, resulting in strong eastward sediment fluxes, under the current conditions [Lucas et al., 2014a; Charnay et al., 2015]. Note that the second hypothesis succeeds in explaining finely the orientation of both dunes and their "defects" as well as the equatorial dune confinement [Lucas et al., 2014a].

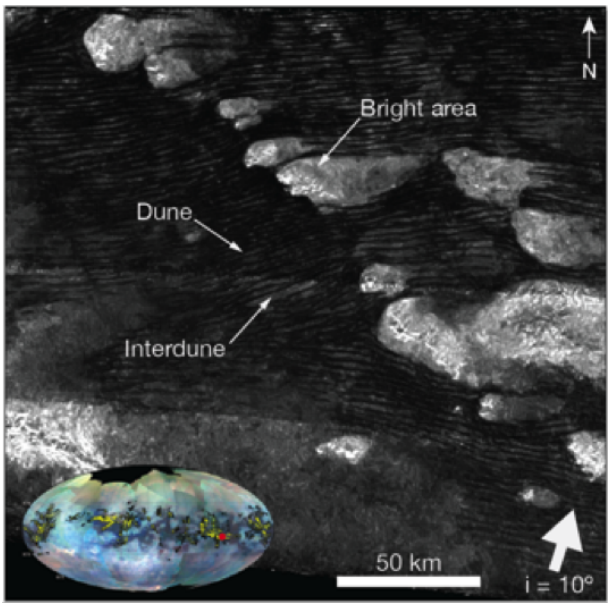

Figure 2: Belet sand sea as observed by the RADAR operating in SAR mode on swath T61 upon denoising (see main text in section 2.2 and Lucas et al. [2014b]). Inset shows the location of Belet at global scale. Individual dunes are distinguishable from interdunes while look direction is roughly normal to the dune's crest orientation (thick white arrow). Radar bright areas, commonly found embedded in Titan's dune fields also named as "inselbergs" are indicated.

Beyond the climatic implications, these two main hypotheses may imply distinguishable dune growth mechanisms and associated morphodynamics hence subsequent sediment transport. Recent numerical simulations [Gao et al., 2015], laboratory experiments [Courrech du Pont et al., 2014], and field measurements [Lancaster and McCarley-Holder, 2013; Ping et al., 2014; Courrech du Pont et al., 2014; Gao et al., 2016] show that under the same multi-directional wind regime, dunes can have two different orientations depending on sediment avail-

ability and granulometry distribution. In the case of a large sediment supply, dune growth can be described as a bed instability that selects the alignment for which the gross bedform-normal transport is maximized [Rubin and Hunter, 1987] (henceforth referred to as the bed instability mode). In contrast, recent works [Reffet et al., 2010; Courrech du Pont et al., 2014] showed that for the case of a limited sediment supply where dunes grow by the transport of sediment over a non-erodible bed (i.e., and/or a coarser sediment bed), finger-like structures extend in the direction of the resultant sediment flux (henceforth referred to as the elongating mode).

Assessing the surface properties in the sand seas, especially of the dunes and their inter-dunes areas (composition, grain size and fraction and depth of sediment cover) is therefore critical, as the type of dune growth mechanism and their resulting orientation will entirely depend on the difference (or not) their respective sediment properties. Without a more precise knowledge of the sediment properties in the inter-dunes and in the dunes, the interpretation given to the observed dune orientation in terms of wind regime and dune activity stays ambiguous. Previous studies already showed that a possible different composition and/or grain size in the inter-dunes compared to the dunes is suggested by infrared VIMS observations [Barnes et al., 2008; Rodriguez et al., 2014; Bonnefoy et al., 2016] and microwave radiometry [Le Gall et al., 2011; Le Gall et al., 2012]. Radar-bright areas are also observed in many regions on Titan. Such radar-bright inselbergs embedded within sand seas suggest distinctive texture and composition of the bedrock beneath the sediment cover. Note that they may reflect various terrains global wide and hence is considered as geomorphic group rather than a single geological unit.

In this study, we aim at assessing the Titan's surface and sub-surface properties at different sand seas from the Cassini RADAR SAR signature. By combining modeling of the microwave backscatter following Paillou et al. [2006, 2014], with the large coverage in incidence angles over the sand seas now available and state-of-the art despeckling technique, we aim at determining the respective surface properties of the dunes, interdunes and inselbergs over threee major sand

seas which are Belet, Shanghri-La and Fensal (Figure 1).

We present the geomorphic classification techniques in section 2. We describe our modeling approach and inversion technique in section 3. We present our results and discuss their implications in section 4, and then conclude in section 5.

2. Geomorphic identification and backscatter signal from SAR data

In this section we describe the data reduction workflow we adopt to extract separately the backscatter cross-section (σ^o) from dunes, interdunes and the radar-bright areas (i.e., inselbergs) throughout the Belet sand sea as example.

2.1. Sand seas as seen by the RADAR SAR imager: Example from Belet

The RADAR instrument operating in the SAR mode provides the highest spatial resolution available of Titan's surface down to 300 m allowing the detection of individual dunes as shown for instance in figure 2 over the Belet sand sea. Besides, some regions have now been observed with a wide range of acquisition geometries in between non-circular Cassini flybys (see figure 3). In particular, Belet has been imaged from 5^o to 55^o of incidence with roughly the four main cardinal directions (i.e., a wide range of look direction) (Figure 3) thanks to the partial overlapping of four RADAR swaths (from Titan's flyby T08, T21, T50 and T61).

This wide range of observation geometry offers an unique opportunity to determine the microwave backscatter function (i.e., σ^o as a function of the incidence angle) and therefore the textural and compositional properties of different terrains. Note that such great range of incidence and look directions are even not available over terrestrial deserts hindering a complete comparison with our work. Nonetheless, related studies on terrestrial terrain are discussed in section 4.

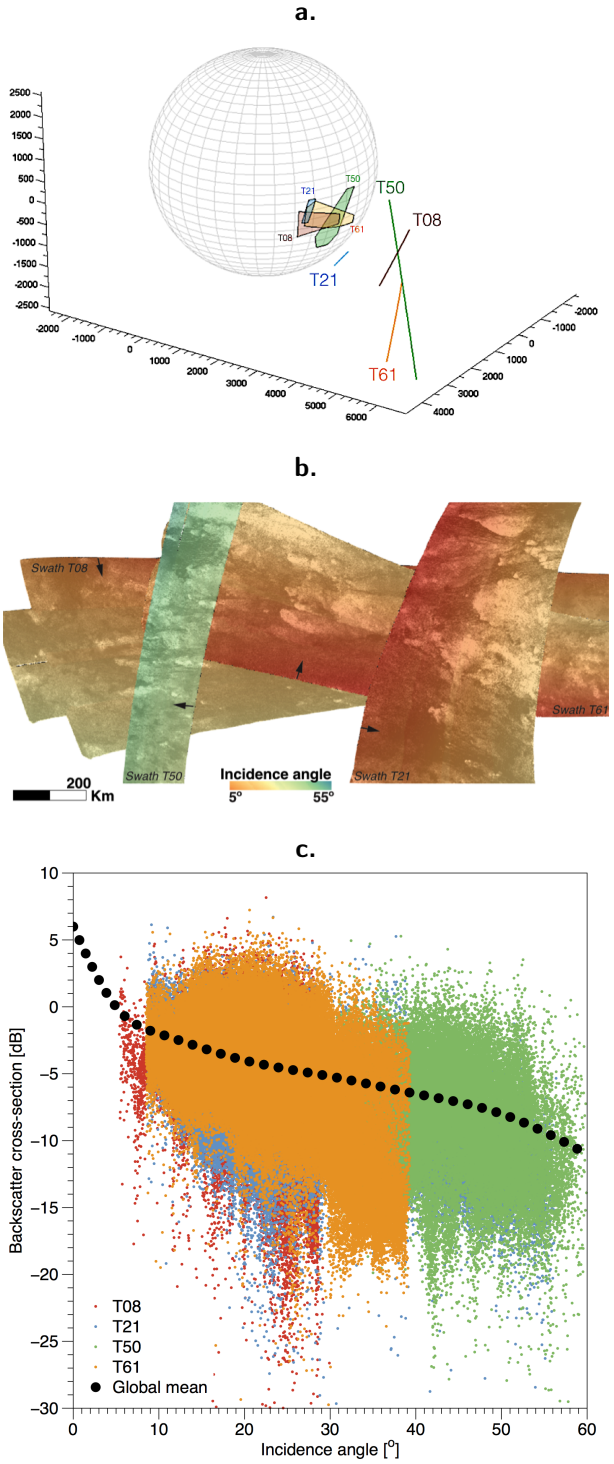

Figure 3: a. Geometries of RADAR observations including footprints and Cassini orbits for T08, T21, T50 and T61 swaths over the Belet sand sea. b. Amplitude backscatter and incidence angle at the associated footprints. Color scales with nominal incidence angle. Black arrows show look direction for each swatch. c. Backscatter cross-section expressed in dB as a function of incidence angle for each individual swath compared to the global mean.

2.2. Data reduction and geomorphic unit classification

Cassini SAR data suffer from speckle noise hindering fine details detection and quantitative analysis [Lucas et al., 2014b]. We hence use the despeckled SAR data, namely NLDSAR (i.e., Non-Local Denoised SAR) in our analysis [Lucas et al., 2014b]. We obtained a significant noise reduction hence data dispersion while being conservative on the mean value as exemplified in figure 4 where backscattering cross-section over T08 swath is shown as a function of the incidence angle.

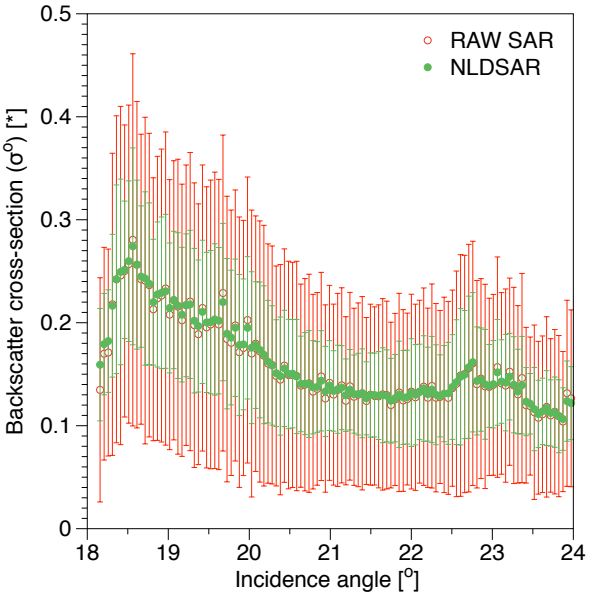

Figure 4: Backscattering cross-section σ^o in physical unit (linear scale) as a function of the incidence angle over a dune fields as observed on T08 swath for RAW (red) and NLDSAR (green) data sets. Dispersion is given for 1 standard deviation.

Taking advantage of the despeckled data, we develop a complete workflow for automatically individually extracting the backscatter functions of dunes, interdunes and bright areas such as inselbergs. Geomorphic unit extraction is performed by a split-spectrum analysis over the SAR data inspired from Daily [1983]. As discussed by this latter study, low spatial frequencies content is due to backscattering signal variations over the surface and subsurface, while high

frequency content is associated to local topographic features. Low pass and high pass filters are hence applied to the image in order to separate low and high spatial frequency information. Additionally one can define a fixed saturation threshold that will control the final brightness in the split-spectrum analysis. This plays a negligible role in the geomorphic unit extraction. Then, the low frequency content can be assigned to the Hue axis, the high frequency content to the Value axis, and the fixed saturation threshold to the Saturation level, resulting in a colored image defined in the Hue-Saturation-Value colorimetric domain. Finally, we convert the H-S-V image into R-G-B domain, resulting in a synthetic colored image based on the spatial frequency content of the σ^o amplitude hereafter named the split-spectrum map. Classification over the split-spectrum map is hence greatly facilitated and it is possible to robustly distinguish geomorphic units such as dunes, interdunes and radar-bright areas (i.e., inselbergs) based on their respective scattering properties. Figure 5 shows the results of our classification for the four swaths covering Belet sand sea.

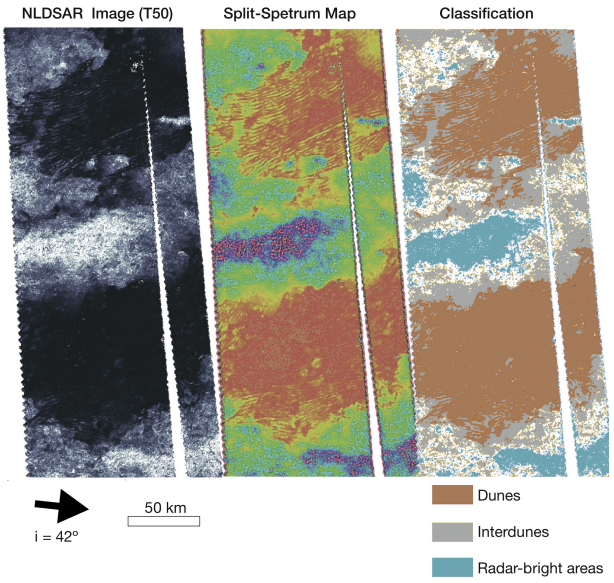

Figure 5: Geomorphic classification upon denoising and split-spectrum analysis over Belet sand sea from T50 swaths. Interdunes (in yellow) are detectable even over the dark areas inside Belet sand sea.

The complete data reduction workflow with the main steps is summarized on figure 6. This work has been applied to Belet, Shanghri-La and Fensal sans seas (Figure 1 and Table A.1 in appendix A1).

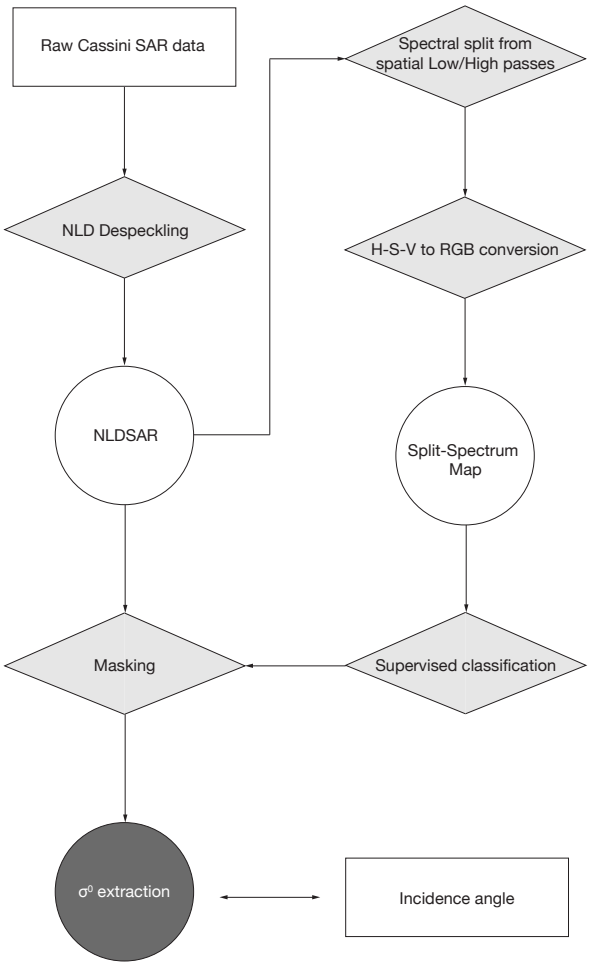

Figure 6: Workflow steps for extracting backscatter signal (σ^0) from despeckling, split-spectrum and supervised classification.

2.3. Extraction of the backscatter as a function of the incidence angle

As shown on figure 3, the Belet sand sea is observed on swath T08, T21, T50 and T61 with a range of 40^o in incidence angle. We compute the mean within

3-sigma dispersion of the backscatter cross-section every half-degree of incidence angle. The mean and dispersion are calculated over thousands of measurements for each considered incidence angle, guarantying the statistical reliability of the extracted functions. This is done for each of the 3 geomorphic units isolated over the Belet sand sea (dunes, interdunes and inselbergs).

Note that the incidence angle of observation is not necessary the local incidence angle especially for the dunes and the inselbergs that are not flat surface. In the case of the dunes, the limited spatial resolution of the SAR images makes the distinction between the two sides of the dunes barely detectable. Nevertheless, in order to provide the maximum constraints, we take into account the glints that are detectable on T08 and T61 and that originate from the reflection of the RADAR waves on the flank of the dunes when specular geometry is met.

The observed backscatter signals as a function of the incidence angle is shown on Figure 9 for the 3 units. We emphasize that these are the first backscatter functions extracted from denoised SAR images that cover such a large range in incidence since the beginning of the Cassini mission.

Interestingly, the microwave backscattering functions of the 3 geomorphic units do not overlap, suggesting significant differences in their surface and subsurface properties. The inselbergs show a rather flat trend with increasing incidence. This is an indication for a very large roughness with respect to the Cassini RADAR wavelength of 2.17 cm [Ulaby et al., 1982]. While showing a lower backscatter cross-section, the interdunes areas also present an almost constant backscatter curve up to an incidence of 50^o. On the contrary, the dunes, which are radar-darker at all incidences than the two other geomorphic units, present a stronger variability with incidence angle (i.e, specular component at low inc angles). This may reflect a textural difference (with a lower roughness), a lower dielectric constant and/or a lower diffuse component [Ulaby et al., 1982]. Nonetheless, the flatness of the three curves between 10° and 50° (e.g., 20° and 50° for the dunes) suggest a significant diffuse component due to roughness or/and volume scattering.

3. Microwave backscatter modeling and inversion results

In this section we first discuss the basics of microwave backscatter modelling and explain our choices for the subsequent inversion from Bayesian inference.

3.1. Microwave backscattering direct models

There is a long-standing development in microwave backscatter modelling for terrestrial applications. Here we based our analysis on previous work that developed models that depend on surface roughness, and the dielectric constant $\epsilon = \epsilon' - j\epsilon"$, accounting for coherent and single-scattering part of the signal [Fung, 1992, 1994; Ulaby et al., 1982; Paillou et al., 2006]. The surface roughness is defined by two empirical statistical descriptors: the root-mean-square height (ξ), quantifying the vertical variations of the surface, and the correlation length (ζ), characterizing the typical horizontal size of surface bumps. Hence considering surface roughness with a Gaussian height distribution and exponential autocovariance function, these are hence defined as:

$$\xi = \sqrt{\frac{\sum_{i=1}^{n}(z_i - \bar{z})^2}{n-1}}, \tag{1}$$

z being the elevation, and

$$\rho_N(\delta) = \frac{1}{\xi^2}\big\langle z(x_i+\delta)z(x_i)\big\rangle, \tag{2}$$

where $\big\langle\big\rangle$ being the averaging operator and δ being the distance between a pair of the considered points. Hence, the correlation length reads

$$\zeta = \rho_N^{-1}(e^{-1}). \tag{3}$$

From very smooth to very rough terrain, 1-layer Integral Equation Method (IEM), (Physical Optics) PO and (Geometrical Optics) GO surface scattering models can be considered, and are defined respectively by :

$$\sigma^0_{IE} = \frac{k e^{-2\kappa^2\xi^2\cos^2(\theta)}}{4}\sum_{n=1}^{\infty}|I^n_{pp}|^2\frac{W^n(-2k\sin(\theta),0)}{n!}, \tag{4}$$

where k is the wave number, and W^n being the Fourier transform of the nth power of the surface correlation function depending of ζ, and with

$$I_{pp}^n = (2k\cos(\theta)\xi)^n f_{pp} e^{-k^2\cos^2(\theta)\xi^2} + \frac{1}{2}(k\cos(\theta)\xi)^n \left[F_{pp}(-k\sin(\theta)) + F_{pp}(k\sin(\theta))\right], \quad (5)$$

with f_{pp} and F_{pp} being the coefficient of the Kirchoff and complementary fields, respectively [Fung, 1994], and

$$\sigma_{PO}^0 = 2\kappa^2\cos(\theta)\Gamma_{pp}(\theta)\exp(-2\kappa\xi\cos(\theta))^2 \times \sum_{n=1}^{\infty} \frac{(2\kappa\xi\cos(\theta))^{2n}}{n!} \int_0^\infty \rho^n(x) J_0(2\kappa x\sin(\theta)) x dx, \quad (6)$$

with J_0, Γ_{pp} and $\rho(x) = \exp(-x^2/\zeta^2)$ being respectively the zeroth-order Bessel function of the first kind, the Fresnel reflectivity and the Gaussian surface autocorrelation function, and

$$\sigma_{GO}^0 = \Gamma(\theta = 0)\frac{\exp(-\tan^2(\theta)/2m^2)}{2m^2\cos^4(\theta)}, \quad (7)$$

with $m = \sqrt{2}\xi/\zeta$ and $\Gamma(\theta = 0)$ being the Fresnel reflectivity at normal incidence. Note that the coherent part of the backscatter is correctly simulated with the GO model which is therefore valid at all incidence. The non-coherent surface scattering model is selected as a function of the roughness domain relative to the RADAR wavelength. For smooth to very rough terrain, IEM, POM and GOM are considered [e.g., Paillou et al., 2006]:

$$\sigma_{Spp}^0 = \begin{cases} \sigma_{IE}^0 & \text{if } k\xi < 3 \text{ and } k^2\xi\zeta < 1.5\sqrt{\epsilon}, \\ \sigma_{PO}^0 & \text{if } k\zeta > 6 \text{ and } k^{-1} < \xi < 0.06k\zeta^2, \\ \sigma_{GO}^0 & \text{if } (2k\xi\cos\theta)^2 > 10 \text{ and } k\zeta > 6. \end{cases} \quad (8)$$

Note that recently, Paillou et al. [2006, 2014] applied these models to the Cassini RADAR SAR data and emphasized i) that Titan's surface is rough, with respect to the RADAR's wavelength, ii) the importance of volume scattering from the subsurface. To account for this effect, we also add a volume scattering term to the surface model which reads:

$$\sigma^0_{Vpp} = \frac{3}{4} a T_{ij}^2 \cos(\theta) \left(1 - e^{-2\tau \cos^{-1}(\theta_t)}\right), \tag{9}$$

where T_{ij} being the Fresnel coefficient and τ the optical depth defined as $\tau = 1/(1\text{-}a)$, with a being the micro-wave albedo. Note that the term σ^0_{Vpp} accounts in fact for the totality of the diffuse part of the backscattering signal, i.e. volume scattering and/or surface multiple-scattering without possibly making the difference between both.

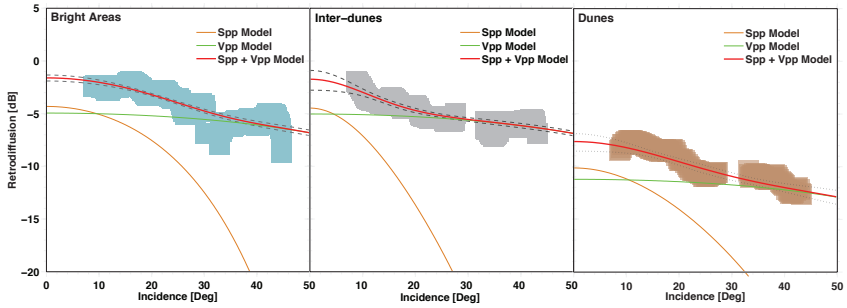

Figure 7: Results of the direct Monte Carlo simulation obtained from the GO model over the sand sea of Belet. The colorized areas correspond to the observed backscatter signal at the three different geomorphic units with a 1-σ standard deviation in width. The contribution of the two terms for the surface (Spp) and volume (Vpp) are shown separately and additively as indicated. The area embraced by the dashed-lines correspond to the best 5% results from the χ^2-tests.

For sake of clarity, it's important to remind few limitations of the considered models. First, note that the domains of validity for the surface term (σ^0_{Spp}) slightly differ throughout the literature [e.g., Paillou et al., 2006; Fung, 1992; Zribi and Dechambre, 2002]. Moreover, it has been shown that for terrestrial terrains, models are not always able to reproduce observations in their respective domain of validity [Zribi et al., 1997, 2000; Zribi and Dechambre, 2002]. Secondly, as recall above, the non-coherent surface scattering depends on statistical descriptors of the surface roughness, which, as defined, are bounded to each other (see Appendix A2). Consequently, they cannot be inversed independently. Thirdly, the ability of these descriptors to characterize natural surface

is, in practice, not obvious, as they depend on the scale at which they are defined (i.e., the length of the roughness profile). Moreover, their interdependence is itself a function of this scale and the nature of the terrain (i.e., rough vs. smooth) [e.g., Baghdadi et al., 2000; Zribi and Dechambre, 2002; Bretar et al., 2013]. Finally, it has been shown that it is much more pertinent to consider the ratio of the two descriptors in order to characterize the roughness of a natural surface, hence seen as root-mean-square slope ($s = \xi/\zeta$). Strictly speaking, from these previous studies, it appears that the ratio ($Z = \xi^2/\zeta$) makes it possible to describe this roughness in a more satisfactory manner.

Although Cassini Radar micro-waves are capable of penetrating beneath the surface, only 1-layer model is considered in this study. The number of unknowns in case of +2-layers model become high and would require additional constraints on the physical properties of Titan's soil that we do not have yet, hence would not provide further insights on the physical properties of Titan's geomorphic units [Paillou et al., 2006]. Consequently, considering the Cassini RADAR wavelength of 2.17 cm and the validity domain for each models, we run 5.10^5 Monte Carlo simulations accounting for 1-layer model with no model parity and found that most of our best fits obtained from a reduced χ^2-tests fall in the very rough terrain domain (i.e., GO model) for the 3 geomorphic units considered over Belet sand sea as shown in figure 7. Note that this compatible with preliminary works [Paillou et al., 2014].

3.2. Sensibility analysis and synthetic tests

The non-linearity and non-homogeneity of the modeling make the physical parameters inversion assessment non-trivial. As we aim at being the most quantitative as possible, we performed a sensitivity analysis from the variance-based Sobol's method that quantifies the amount of variance that each parameter contributes to the unconditional variance of the model output Sobol' [1993]. These amounts, caused either by a single parameter or by the interaction of two and more parameters, are expressed as sensitivity index, which represent fractions of the unconditional model output variance. The case for a very rough surface (i.e.,

GOM domain) is shown on figure 8 for all physical parameters considered. Our sensibility analysis exemplifies quantitatively what is suggested in figure 7: the surface RMS slope is dominating at low incidence, while the albedo dominates at higher angles. Additionally, contribution of the real part of the dielectric constant remains lower (<0.20), while GO model is not sensitive to the imaginary part. However, the uncertainties emphasize that even low-contribution parameters can still be assessed as long as the coverage in incidence is sufficient.

In order to compute the marginal posterior probability of each physical parameter, we use a Bayesian statistical model and fitting algorithms based on Markov chain Monte Carlo inversion (MCMC). In order to assess the capability of the method to retrieve the physical parameters, synthetic tests are done and exemplified in figure 8. Backscatter signal is computed from the GO model ((7) + (9)) and with $\epsilon' = 1.55$, $s = \xi/\zeta = 0.10$, and $a = 0.30$ for different incidence angles somewhat taken randomly with significant gaps between 30° and 50°. Gaussian noise is added on the mean values independently for each incidence angle considered with a standard deviation of 0.3 dB. Uncertainties are simulated from a uniform distribution with 1-σ at 0.6 dB. We therefore obtained realistic data that mimic the actual data from Cassini SAR (figures 7 and 8 and Appendix A3). As shown on the example in figure 8, true parameters are correctly assessed by the method.

3.3. Surface properties from Bayesian inference

Relying on this complete and robust approach, we hence perform a Bayesian inference using the GO model, in order to characterize the physical parameters s, ϵ' and a which reflect the surface roughness (i.e., RMS slope), the composition and porosity of the terrain as well as the subsurface contribution respectively. This analysis has been done over 50.10^6 runs of the GOM over $\epsilon' \in$ [1,5], $s \in$ [0.001,5], and $a \in [0.0, 1.0]$. Optimal fits and 95% confidence intervals (CI) are shown for the considered terrains on figure 9. In all cases, the 95% CI's fall into the observed dispersion, even when the incidence coverage is low. The mean observed data are correctly retrieved by our simulation.

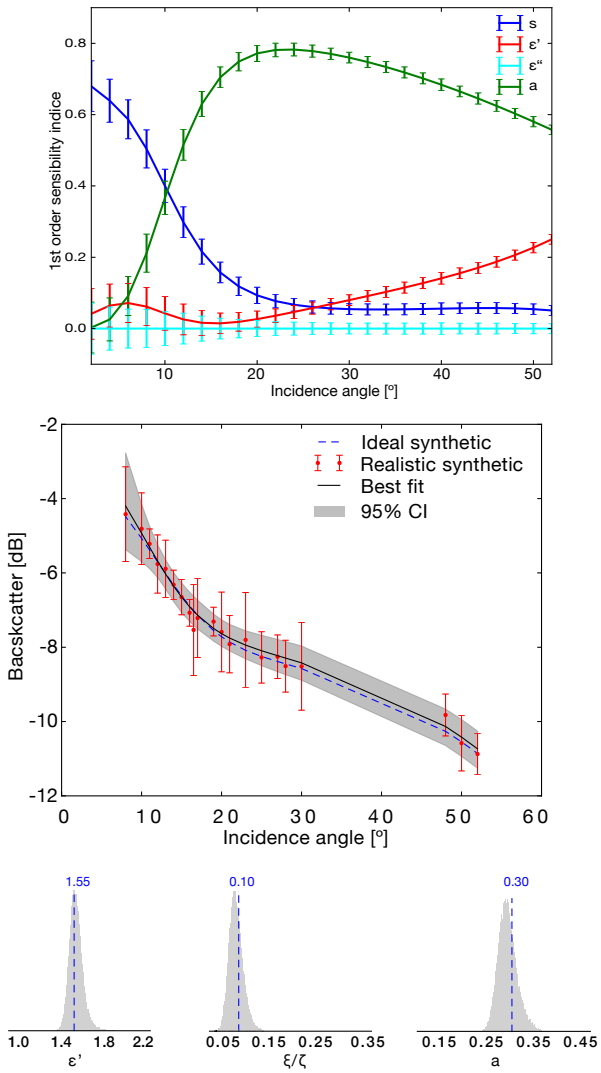

Figure 8: Sensibility analysis of the micro-wave backscatter function. (top) Sobol analysis of the GOM model. At low incidence (i<18°), the surface roughness through the root-mean-square slope s dominates, while at higher incidence, the albedo a that determines the volume scattering contribution dominates the backscatter signal. (bottom) Bayesian inference from the GO model on synthetic data. Ideal curve is obtained from equations (7) and (9) with $\epsilon' = 1.55$, $s = \xi/\zeta = 0.10$ and $a = 0.30$. Gaussian noise is added to the mean values and uniform noise is added to the errors. The best fit with it 95% confidence interval is shown. Marginal posterior probability for each parameters are compared with true values before noise is added. The respective search ranges are $\epsilon' \in [1; 5]$, $s \in [0.005; 0.6]$ and $a \in [0.1; 1.0]$. For sake of clarity, respective ranges are tightened.

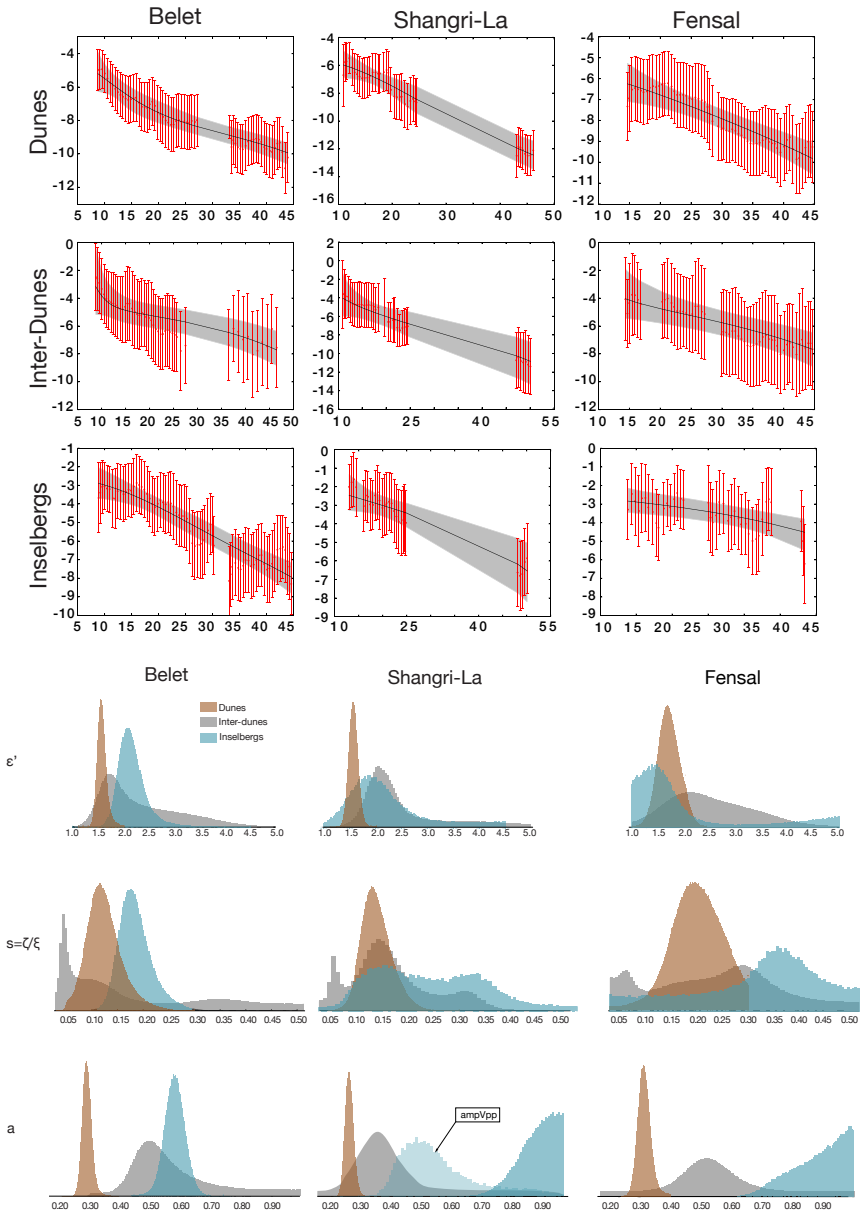

Figure 9: Bayesian inference of physical properties over Titan's sand seas. (top) Backscatter (expressed in dB) as a function of the incidence angle (in degrees) for the dunes, the inter-dunes and inselbergs (in red) with associated Markov chain Monte Carlo inversion (plain dark curves). The 95% CI are represented by the gray area. (bottom) Marginal posterior probability of the dielectric constant ϵ', the surface roughness expressed as $s = \zeta/\xi$, and the albedo a for the considered terrains. Each marginal posterior probability is computed from Markov chain Monte Carlo inversion over 10 millions of runs independently.

The resulting marginal posterior probabilities computed from our Bayesian analysis for each physical parameter are summarized in figure 9. We obtain purely Gaussian posterior probabilities for the dunes for each parameter for the three considered sand seas (ϵ', ξ/ζ, and a). Qualitatively, the resulting distributions are very similar and emphasize the homogeneity of the dune's material at the global scale (i.e. within the equatorial belt). Situation is subtler in the case of inter-dunes and bright areas. The shapes of their respective marginal posterior probabilities indicate that for all of the considered physical parameters there terrains reflect more complex media with distinctive contributions. They also reflect an important variability of surface properties from one place to another. Note that while brigh-areas are extracted from Inselbergs solely for Belet, they correspond to wider areas, hence more heterogeneous for Shangri-La and Fensal sand seas which both bound Xanadu (Figure 1).

In details, the real part of the dielectric constant (ϵ') strongly differ between the geomorphic units. For Belet sand seas, while the distribution shape is Gaussian for the dunes with a mean value around 1.6, we obtained a spread distribution with a peak at $\sim$1.75 and an mean value around $\sim$2.2, similarly to the bright-areas, which have a Gaussian distribution. This latter differs from one place to another, which is may reflect global variations between the regions of interest studied. This also may be subsequent to the poor coverage we obtained over Fensal, which differ strongly from the two others. We also note that dunes in Fensal slightly differ from Belet ans Shangri-La. This may reflect latitudinal and altimetric controls of Titan's dune field morphometry as shown by [Le Gall et al., 2012]. Essentially, the overall results with respect to the dielectric constant inversion show that i) dunes are compatible with a very homogeneous sand made of porous organics, ii) bright-areas and inter-dunes are a mixture of contaminated water-ice with tholins in different ratios, which is a direct confirmation of what was previously suggested from passive microwave and infrared observations [Janssen et al., 2016; Le Gall et al., 2011; Barnes et al., 2008; Soderblom et al., 2007] as well as laboratory experimentsPaillou et al. [2008]. However, more specific details that cannot be assessed with our

approach and available data from Cassini RADAR.

Regarding the surface roughness assessed through the RMS slope (ξ/ζ), we show that here again, dunes appear very homogeneous all over the regions of interest, with a subtle difference for Fensal. This is interpreted similarly to the dielectric constant discussed above, and may reflect geographical controls on dune's field morphometry, but overall, dunes appear extremely smooth. Inter-dunes and bright-areas show wider surface roughness distributions over the three regions of interest. This may reflect multi-scale roughness variations compatible with either mountainous terrains or sedimentary plains made of a non-homogeneous granulometry. This distinct roughness is a critical result as is may reflect differences in grain size, which is compatible with recent analysis in the IR spectra from VIMS instrument [Bonnefoy et al., 2016].

Finally, the contribution of the volume scattering throughout the micro-wave albedo a reflect that dunes strongly attenuate the Radar signal, while inter-dunes and bright-areas reflect a significant sub-surface component. This agrees with the two other parameters inversions hence a bedrock contribution beneath these terrains covered by organics sediments as it is suggested by unresolved radiometry [Le Gall et al., 2011; Le Gall et al., 2012] and IR from VIMS [Barnes et al., 2008]. Note that albedo is reaching its saturation value for some brigh-areas (i.e., particularly for Shangri-La and Fensal), and hence an amplification of the diffuse part of the backscattering signal is required (see ampVpp on figure 9) as suggested by Janssen et al. [2016].

To summarize, our Bayesian inferences emphasize the homogeneity of the dunes units while inter-dunes and bright areas are composed of complex terrains reflecting both geographical variations and strong sub-surface contribution. Ultimately, this argues in favor of contributions of different surface and subsurface properties at the spatial resolution of the SAR instrument that would require multi-layer model with complex mix but would required additional constraints (i.e. inter-layer Fresnel reflexions, non-isotropic porosity/fracturing, potential presence of alkanofer beneath the surface, grain size distribution etc.) for being considered useful for Bayesian inference without which, it would be unlikely ca-

pable of providing new insights. Therefore such modelisation is out of scope of this work. Nonetheless note that such spatial variations in surface and potentially subsurface properties have been already discussed in Lucas et al. [2014b] as it appears that patches of different backscatter function are detected upon denoising of the SAR data (see supplementary information of [Lucas et al., 2014b] for a detailed discussion).

Nevertheless, our analysis shows a clear distinction in roughness, composition, porosity and isotropy between dunes and micro-wave brighter units such as inter-dunes and Inselbergs on Titan. Implications in terms of aeolian system morphodynamics are discussed in the following section.

4. Discussion

Along with the wind regime, sediment supply has a critical control on dune morphodynamics [Gao et al., 2015, 2016; Rubin and Hunter, 1987; Ping et al., 2014; Courrech du Pont et al., 2014; Lucas et al., 2015]. Therefore, while we have very limited understanding of current and past wind conditions on Titan, our results showing a distinguishable physical properties between dunes and their inter-dunes have important implications in terms of dune morphodynamics as well as climatic conditions.

Isolated dunes evolve by recycling their own sediment at the crest. Hence, their sedimentary structure reflects the wind regime responsible of their own formation. However, this stigma is limited to a short period of time. At the scale of a sand seas that cover large areas, morphologies integrate climatic cycles punctuated by alternations of that is to say arid and humid periods. Therefore, it is challenging to determine if a sand seas is at the equilibrium with contemporary wind regimes or whether it is at a transient state reflecting different wind regimes integrated over time [McDonald et al., 2016; Lucas et al., 2014a].

On Earth, sand seas with dunes elongating over tens of kilometers are observed in the Ténéré desert (Niger) or in the Kumtagh desert (China) (see Figure 10). In both cases, linear dunes form extending sand cords aligned with

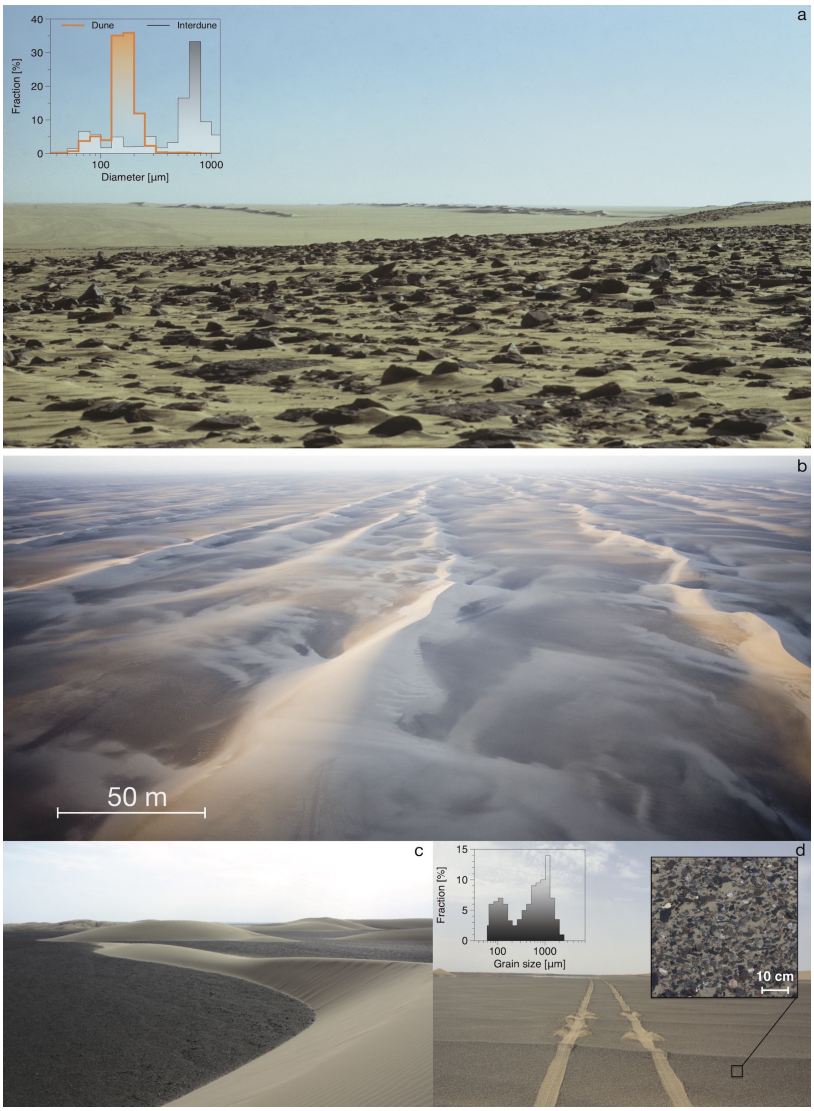

Figure 10: Examples of size segregation by selective transport and avalanches in (a) Ténéré Desert, Niger, (b-d) in the Kumtagh Desert, China. Grain size in inter-dunes is 5 to 20 times larger than in the dunes. The surface roughness is 1 to 2 orders of magnitude higher in the interdunes. Granulometry comes from Lucas et al. [2015] for Niger and Qian et al. [2015] for China. Photographs credits: Niger, Y. Callot, (1976) - China, G. Steinmetz and C. Narteau, (2016).

the residual drift direction [Lucas et al., 2015; Ping et al., 2017]. These linear dunes are periodically indented by secondary structures (i.e., ejecting barchans). A long standing explanation have invoked past changes in wind orientations. In both cases, recent works have shown that actually non-symmetric wind regimes (like those measured nowadays in these areas) are responsible of the observed patterns and that these extending dunes with secondary bedforms are stationary aeolian system that satisfy contemporary wind regime implying a stable climatic conditions over the sand seas formation [Ping et al., 2017].

Indeed, it is well known that either by gravity and/or by shear flow, granular systems are good at segregation during avalanching and selective transport respectively [e.g. Makse et al., 1997; Cizeau et al., 1999]. It has been recently shown that the ratio between fine and coarse grains controls the segregation mechanisms leading to the formation of an armor layer [Gao et al., 2016]. This latter controls both sediment supply and sediment transport as larger particles composing almost exclusively the inter-dune areas becomes essentially immobile or contribute poorly to the sediment fluxes. Such granular segregation is observed in these terrestrial sand seas (see insets in figure 10).

Accordingly to these terrestrial consideration, our results suggest that Titan's dunes are developing either over a coarser sediment bed, i.e. sediment segregation. As discussed previously, infrared and microwave analyses are not incompatible with a thin layer of sediment in between the dunes, if grain sizes strongly differ. Although there is no direct link between the grain size and the surface roughness, the RMS slope we found in the inter-dunes areas is compatible with a sediment bed made of different grain sizes. Additionally, the "defects" depicted in Ewing et al. [2015] would be similar to those observed in the Kumtagh (Figure 10, and [Ping et al., 2017]).

Consequently, based on our findings, Titan's interdunes may be composed of an armor layer of fine and coarser grains with respect to the dunes. Linear dunes made of finer grain hence propagate over a flat armor layer similarly to sand seas in Niger and China [Gao et al., 2016; Lucas et al., 2015; Qian et al., 2015; Ping et al., 2017]. This interpretation is therefore in good agreement

with the elongating growth mechanism proposed by Lucas et al. [2014a] under the current wind conditions accounting for equinoctial strong winds from either gusts and/or storms [Tokano, 2010; Charnay et al., 2015].

5. Conclusions

Micro-wave backscatter function from Cassini SAR data has been derived and analyzed over the sand seas in the equatorial belt of Titan. First, we show that, backscatter function from inter-dunes is clearly distinguishable from the dune's. This is reflecting a difference in composition and attenuation as well as surface roughness. Our findings are compatible with hyper-spectral observations from VIMS instruments. As demonstrated by a Markov chain Monte Carlo inversion, as opposed to the dunes, interdunes present a higher surface roughness, a slightly higher dielectric constant and stronger subsurface contribution. These properties reflect a thin sediment bed made of a mixture of fine and coarser grains over an icy crust polluted by organics. As for the dunes, our results confirm that the dunes are composed of organics uniquely and are very homoegenous at the gloabal scale. The surface roughness we derived is compatible with the presence of secondary bedforms, such as ripples and avalanches. The physical properties of the studied Titanian sand sea suggest that interdunes play as an armor layer in between the linear dunes. This may reflect a strongly different contribution in the sediment flux, as coarser grain would need higher shear stress to be moved, similarly to what is observed in Niger or China where linear dunes elongate along the resultant drift direction under a multi-directional wind regime. This resulting morphodynamics is therefore compatible with the elongating growth mechanism that has been proposed by Lucas et al. [2014a]. Indeed, unless current wind regime at Titan's surface is bi-modal and purely symmetric which is unlikely due to non-circular orbit, topography, and albedo variations, one can expect a reorientation of dune crest between depleted and/or coarser inter-dunes case and the case of covered dense inter-dunes that can contribute to the linear dunes growth as observed in Rub' al Khali as well as in

the northern hemisphere on Mars for instance. Additionally, the different dune shapes observed (e.g., raked linear dunes, star dunes, asymmetric barchans, see Radebaugh [2013]; Lucas et al. [2014a]; Ewing et al. [2015] clearly suggest the presence of a complex wind regime at Titan's equatorial region, again compatible with our results.

Consequently, sand seas on Titan appear to be evolving under a complex aeolian systems, with dune pattern coarsening and interdunes armoring similarly to their terrestrial analogues either in Saudi Arabia, Niger or China. Following our study, further investigation on local properties accounting for azimuthal variation of the backscatter function is now necessary for assessing orientation of potential secondary bedforms (i.e., ripples) and their sub-sequent secondary winds. Besides the equatorial sand seas, our method allows us to retrieve quantitatively with the highest spatial resolution the surface properties as detected in microwave from different geomorphic units, such as plains, badlands, mountainous, fluvial, and lacustrine terrains, hence allowing further investigation in Titan's geological and climatic processes.

Acknowledgments and Data

No author declares conflicts of interests. Cassini SAR data are available on the PDS. Due to the large file size, NLDSAR data set is available upon request by contacting the corresponding author. We thank Stéphane Jacquemoud, Sebastien Labarre and Leon Sylvain for their fruitful inputs that contribute to improve this work. Authors also thank the Cassini Radar Science Team for constructive feedbacks during the elaboration of this research. Author thank Y. Callot and G. Steinmetz for providing field pictures from Niger and China, respectively.

Author acknowledge the financial support of the UnivEarthS Labex program at Sorbonne Paris Cité (ANR-10-LABX-0023 and ANR-11-IDEX-0005-02), the ANR EXODUNES, Space Campus from Université Paris Diderot, the Nvidia Academic Research Support program as well as the CNES.

Appendix

A1. Cassini SAR data summary

Table A.1: Summary of SAR data used in this study

Location	**Swath**	**Inc. angle (θ)**	**Range dir. (WRT-North)**
Belet			
	T08	[5-32]	175
	T21	[10-55]	105
	T50	[30-60]	280
	T61	[8-40]	15
Shangri-La			
	T13		
	T57		
	T58		
Fensal			
	T17		
	T25		
	T29		
	T77		

A2. Surface roughness of natural terrains

As discussed in the main text, statistical descriptors of natural surface roughness depends on the scale and the nature of the considered terrain. Here are combined RMS height (ξ) and correlation length (ζ) from literature and photogrammetric survey on agriculture terrains performed by the corresponding author (Figure A.1). These terrains exemplify the range of surface roughness observed in nature and as to be compared with respect to value retrieved in this study. Note that there is no direct link between the nature of the terrain ans its surface roughness as this later is controlled by different processes that sculpt the topography. Also, multi-scale effects of the surface roughness is known to play

a significant role on the radiometry [Labarre and Jacquemoud, Under review]. Nevertheless, further investigation is required and is currently out of scope of this paper.

A3. Synthetic tests on surface physical properties and subsequent micro-wave backscatter cross-section

Synthetic tests are done in order to show the effect of spatial variations of the physical properties that control the micro-wave backscatter signal (σ^0). Synthetic maps are generated (Figure A.2) and the resulting σ^0. Multiplicative speckle noise with a gamma distribution has been considered based on noise estimation performed in Lucas et al. [2014b].

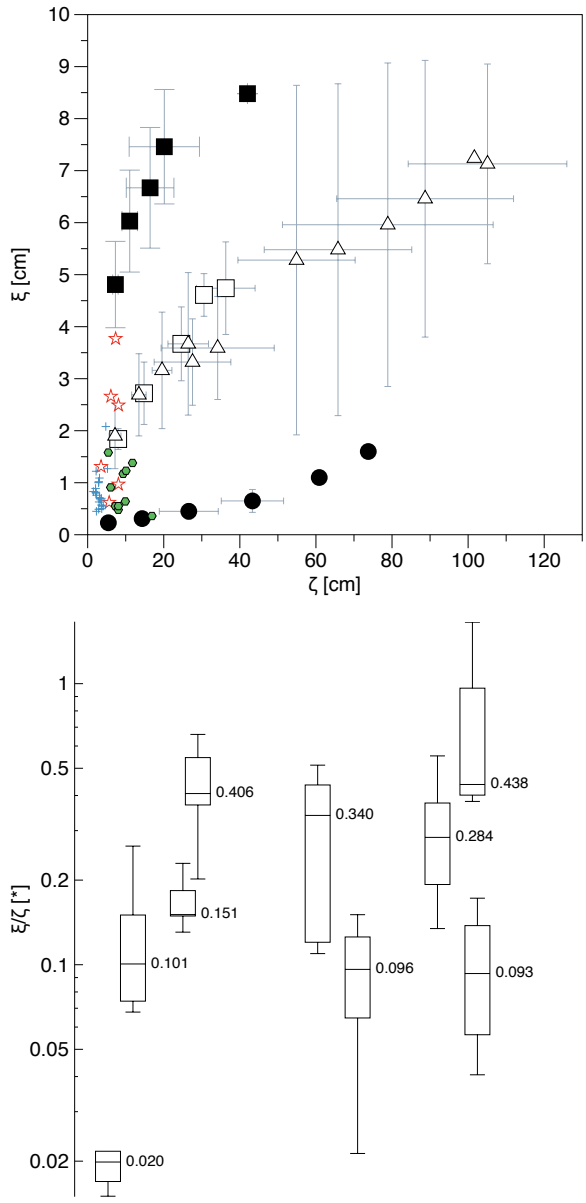

Figure A.1: Natural surface roughness statistics for argiculture and lava terrains. Data are collected from Baghdadi et al. [2000]; Zribi et al. [1997, 2000]; Bretar et al. [2013] and UAV photogrammetric survey performed over agriculture terrain performed in October 2016 by corresponding author.

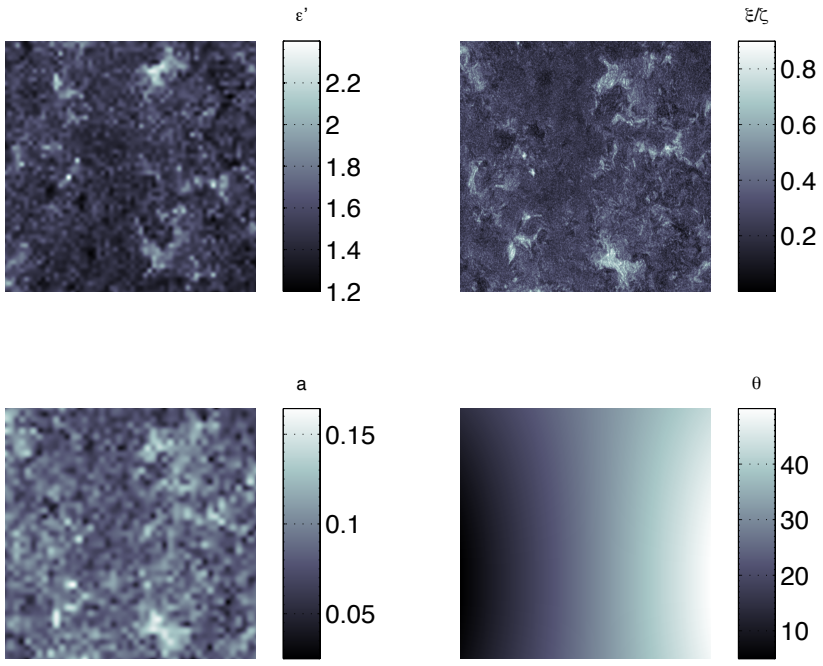
ε'
2.2
2
1.8
1.6
1.4
1.2
ξ/ζ
0.8
0.6
0.4
0.2
a
0.15
0.1
0.05
θ
40
30
20
10

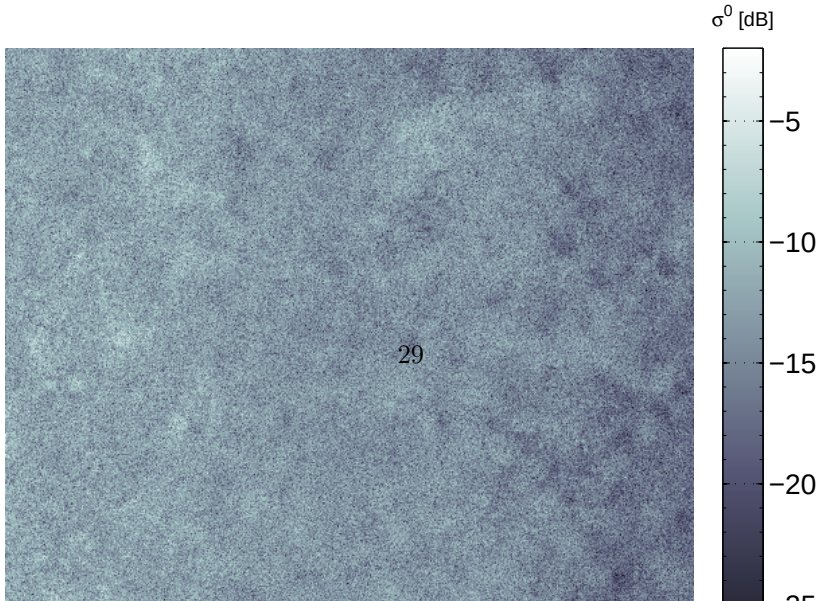
σ0 [dB]
−5
−10
−15
−20
−25

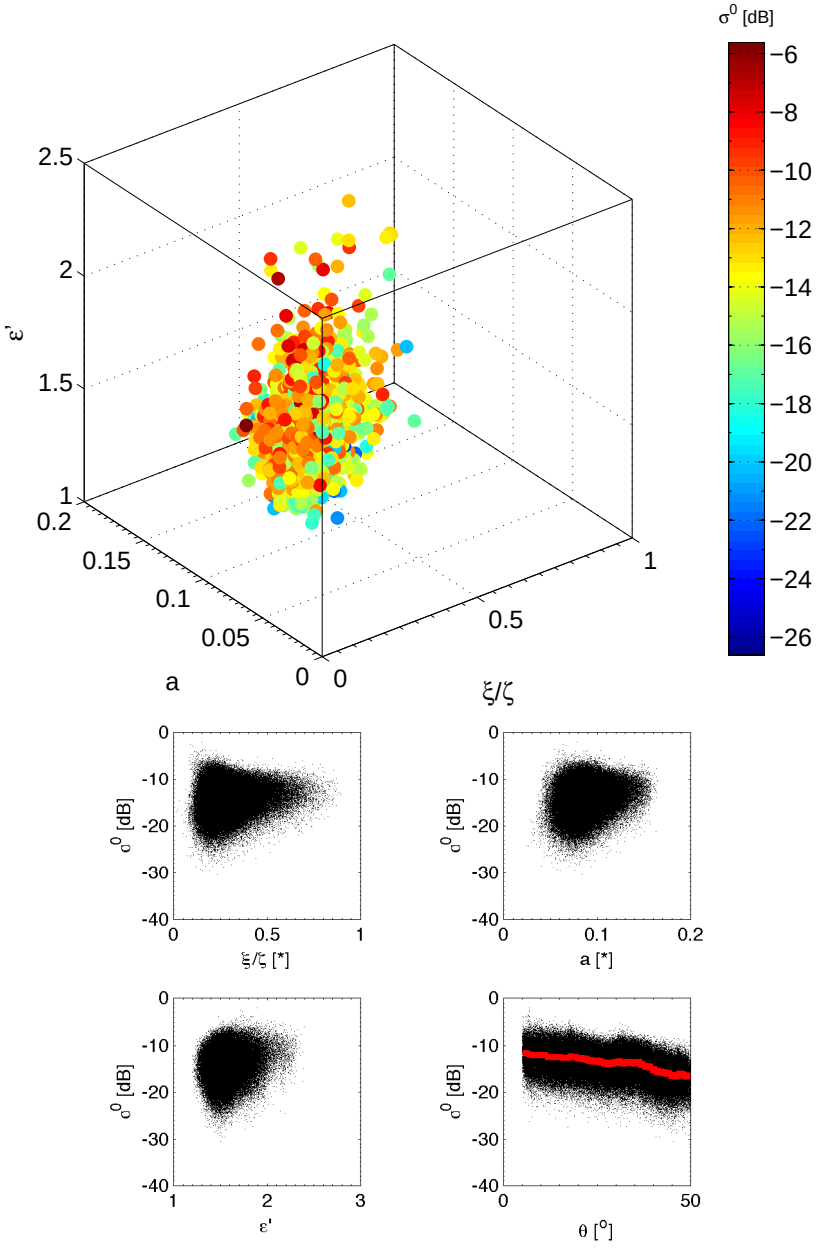

Figure A.3: Respective dependencies of ϵ', ξ/ζ, and a on the resulting σ^0.

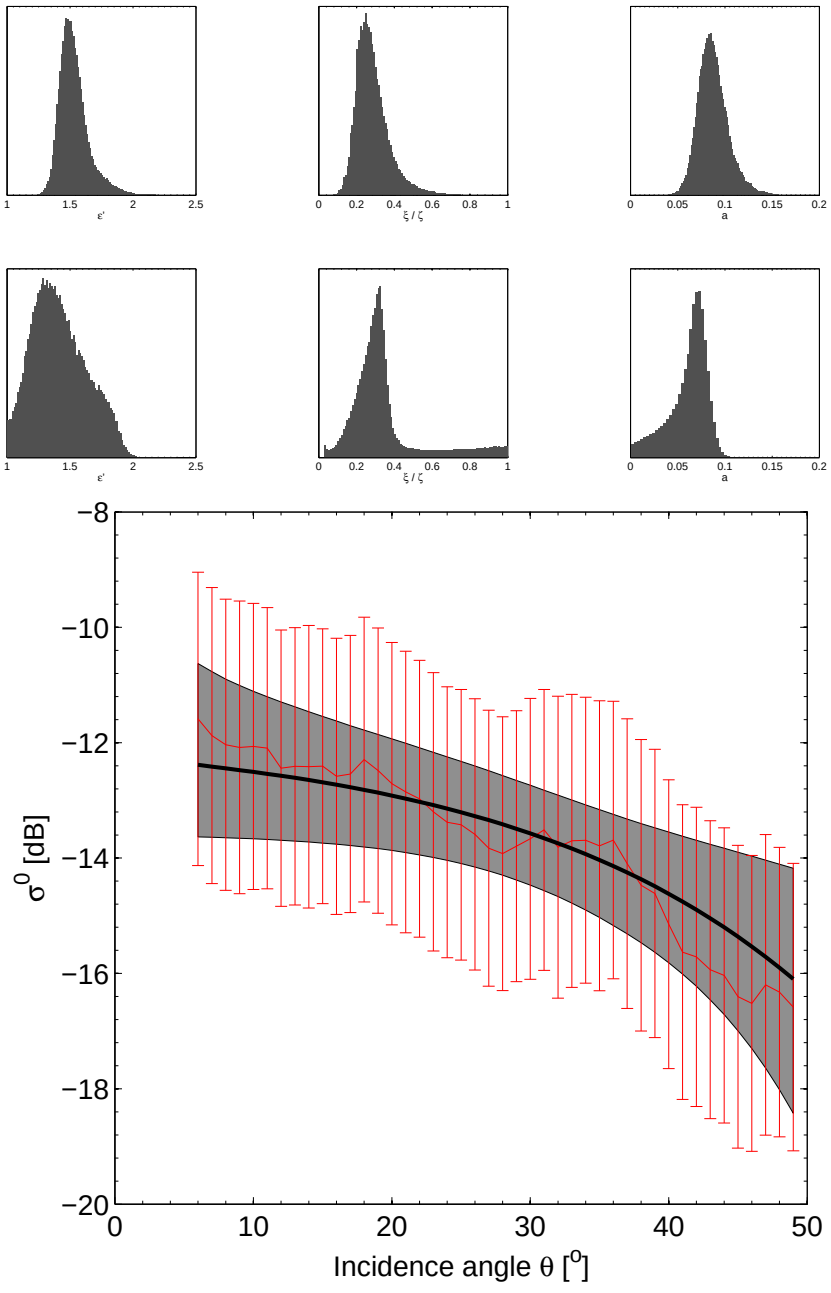

Figure A.4: Respective distribution of ϵ', ξ/ζ, and a.

References

References

Aharonson, O., Hayes, A. G., Hayne, P. O., Lopes, R. M., Lucas, A., Perron, J. T., 2014. Interior, Surface, Atmosphere, and Space Environment. Cambridge Planetary Science, Cambridge, Ch. Titan's surface geology.

Baghdadi, N., Paillou, P., Grandjean, G., Dubois, P., Davidson, M., 2000. Relationship between profile length and roughness variables for natural surfaces. International Journal of Remote Sensing 21 (17), 3375–3381.

Barnes, J. W., Brown, R. H., Soderblom, L., Sotin, C., Mouèlic, S. L., Rodriguez, S., Jaumann, R., Beyer, R. A., Buratti, B. J., Pitman, K., Baines, K. H., Clark, R., Nicholson, P., 2008. Spectroscopy, morphometry, and photoclinometry of titan's dunefields from cassini/vims. Icarus 195 (1), 400 – 414.

Bonnefoy, L. E., Hayes, A. G., Hayne, P. O., Malaska, M. J., Gall, A. L., Solomonidou, A., Lucas, A., 2016. Compositional and spatial variations in titan dune and interdune regions from cassini VIMS and RADAR. Icarus 270, 222 – 237.

Bretar, F., Arab-Sedze, M., Champion, J., Pierrot-Deseilligny, M., Heggy, E., Jacquemoud, S., 2013. An advanced photogrammetric method to measure surface roughness: Application to volcanic terrains in the piton de la fournaise, reunion island. Remote Sensing of Environment 135, 1 – 11.

Charnay, B., Barth, E., Rafkin, S., Narteau, C., Lebonnois, S., Rodriguez, S., Courrech du Pont, S., Lucas, A., may 2015. Methane storms as a driver of Titan's dune orientation. Nature Geosci 8 (5), 362–366.

Cizeau, P., Makse, H. A., Stanley, H. E., 1999. Mechanisms of granular spontaneous stratification and segregation in two-dimensional silos. Phys. Rev. E 59.

Courrech du Pont, S., Narteau, C., Gao, X., 2014. Two modes for dune orientation. Geology 42 (9), 743–746.

Daily, M., 1983. Hue-saturation-intensity split-spectrum processing of seasat radar imagery. Photogrammetric Engineering and Remote Sensing 49(3), 349–355.

Elachi, C., Allison, M. D., Borgarelli, L., Encrenaz, P., Im, E., Janssen, M. A., Johnson, W. T. K., Kirk, R. L., Lorenz, R. D., Lunine, J. I., Muhleman, D. O., Ostro, S. J., Picardi, G., Posa, F., Rapley, C. G., Roth, L. E., Seu, R., Soderblom, L. A., Vetrella, S., Wall, S. D., Wood, C. A., Zebker, H. A., 2004. Radar: The cassini titan radar mapper, in: The cassini-huygens mission: Orbiter remote sensing investigations. Springer Netherlands, 71–110.

Ewing, R. C., Hayes, A. G., Lucas, A., 2015. Sand dune patterns on Titan controlled by long-term climate cycles. Nature Geosci 8 (1), 15–19.

Fung, A. K., 1992. Backscattering from a randomly rough dielectric surface. IEEE Trans. Geosci. Remote Sens. 30, 356–369.

Fung, A. K., 1994. Microwave scattering and emission models and their applications. Artech House, Norwood, Mass.

Gao, X., Narteau, C., Rozier, O., 2015. Development and steady states of transverse dunes: A numerical analysis of dune pattern coarsening and giant dunes. Journal of Geophysical Research 120, 2200–2219.

Gao, X., Narteau, C., Rozier, O., 2016. Controls on and effects of armoring and vertical sorting in aeolian dune fields: A numerical simulation study. Geophysical Research Letters 43, 2614–2622.

Janssen, M., Gall, A. L., Lopes, R., Lorenz, R., Malaska, M., Hayes, A., Neish, C., Solomonidou, A., Mitchell, K., Radebaugh, J., Keihm, S., Choukroun, M., Leyrat, C., Encrenaz, P., Mastrogiuseppe, M., 2016. Titan's surface at 2.18-cm wavelength imaged by the cassini {RADAR} radiometer: Results and

interpretations through the first ten years of observation. Icarus 270, 443 – 459.

Labarre, S. ans Ferrari, C., Jacquemoud, S., Under review. Surface roughness retrieval by inversion of the hapke model: A multiscale approach. Icarus.

Lancaster, N., McCarley-Holder, G., 2013. Decadal-scale evolution of a small dune field: Keeler dunes, california, 1944–2010. Geomorphology 181, 281–291.

Le Gall, A., Hayes, A., Ewing, R., Janssen, M., Radebaugh, J., Savage, C., Encrenaz, P., the Cassini Radar Team, 2012. Latitudinal and altitudinal controls of titan's dune field morphometry. Icarus 217, 231–242.

Le Gall, A., Janssen, M., Wye, L., Hayes, A., Radebaugh, J., Savage, C., Zebker, H., Lorenz, R., Lunine, J., Kirk, R., Lopes, R., Wall, S., Callahan, P., Stofan, E., Farr, T., the Cassini Radar Team, 2011. Sar, radiometry, scatterometry and altimetry observations of titan's dune fields. Icarus 213, 608 – 624.

Lebonnois, S., Burgalat, J., Rannou, P., Charnay, B., 2012. Titan global climate model: A new 3-dimensional version of the {IPSL} titan {GCM}. Icarus 218 (1), 707 – 722.

Lorenz, R. D., Claudin, P., Radebaugh, J., Tokano, T., Andreotti, B., 2010. A 3 km boundary layer on titan indicated by dune spacing and huygens data. Icarus 205, 719 – 721.

Lorenz, R. D., Wall, S., Radebaugh, J., Boubin, G., Reffet, E., Janssen, M., Stofan, E., Lopes, R., Kirk, R., Elachi, C., Lunine, J., Mitchell, K., Paganelli, F., Soderblom, L., Wood, C., Wye, L., Zebker, H., Anderson, Y., Ostro, S., Allison, M., Boehmer, R., Callahan, P., Encrenaz, P., Ori, G. G., Francescetti, G., Gim, Y., Hamilton, G., Hensley, S., Johnson, W., Kelleher, K., Muhleman, D., Picardi, G., Posa, F., Roth, L., Seu, R., Shaffer, S., Stiles, B., Vetrella, S., Flamini, E., West, R., 2006. The sand seas of titan: Cassini radar observations of longitudinal dunes. Science 312 (5774), 724–727.

Lucas, A., Aharonson, O., Deledalle, C., Hayes, A. G., Kirk, R., Howington-Kraus, E., 2014b. Insights into titan's geology and hydrology based on enhanced image processing of cassini radar data. Journal of Geophysical Research: Planets 119 (10), 2149–2166.

Lucas, A., Narteau, C., Rodriguez, S., Rozier, O., Callot, Y., Garcia, A., Courrech du Pont, S., 2015. Sediment flux from the morphodynamics of elongating linear dunes. Geology 43 (11), 1027–1030.

Lucas, A., Rodriguez, S., Narteau, C., Charnay, B., du Pont, S. C., Tokano, T., Garcia, A., Thiriet, M., Hayes, A. G., Lorenz, R. D., Aharonson, O., 2014a. Growth mechanisms and dune orientation on titan. Geophysical Research Letters 41 (17), 6093–6100.

Makse, H. A., Havlin, S., King, P. R., Stanley, H. E., 1997. Spontaneouos stratification in granular mixtures. Nature 386, 379–382.

Mastrogiuseppe, M., Poggiali, V., Seu, R., Martufi, R., Notarnicola, C., 2014. Titan dune heights retrieval by using cassini radar altimeter. Icarus 230, 191 – 197.

McDonald, G. D., Hayes, A. G., Ewing, R. C., Lora, J. M., Newman, C. E., Tokano, T., Lucas, A., Soto, A., Chen, G., 2016. Variations in titan's dune orientations as a result of orbital forcing. Icarus 270, 197 – 210, titan's Surface and Atmosphere.

Neish, C., Lorenz, R., Kirk, R., Wye, L., 2010. Radarclinometry of the sand seas of africa's namibia and saturn's moon titan. Icarus 208 (1), 385–394.

Paillou, P., Bernard, D., Radebaugh, J., Lorenz, R., Le Gall, A., Farr, T., 2014. Modeling the {SAR} backscatter of linear dunes on earth and titan. Icarus 230, 208 – 214, third Planetary Dunes Systems.

Paillou, P., Crapeau, M., Elachi, C., Wall, S., Encrenaz, P., 2006. Models of synthetic aperture radar backscattering for bright flows and dark spots on titan. Journal of Geophysical Research: Planets 111.

Paillou, P., Lunine, J., Ruffié, G., Encrenaz, P., Wall, S., Lorenz, R., Janssen, M., 2008. Microwave dielectric constant of titan-relevant materials. Geophysical Research Letters 35 (18).

Ping, L., Narteau, C., Dong, Z., Rozier, O., du Pont, S. C., 2017. Unravelling raked linear dunes to explain the coexistence of bedforms in complex dunefields. Nature Communications 8.

Ping, L., Narteau, C., Dong, Z., Zhang, Z., Courrech du Pont, S., feb 2014. Emergence of oblique dunes in a landscape-scale experiment. Nature Geosci 7 (2), 99–103.

Qian, G., Dong, Z., Zhang, Z., Luo, W., Lu, J., Yang, Z., 2015. Morphological and sedimentary features of oblique zibars in the kumtagh desert of northwestern china. Geomorphology 228, 714 – 722.

Radebaugh, J., 2013. Dunes on saturn's moon titan at the end of the cassini equinox mission. Aeolian Research 11, 23 – 41.

Radebaugh, J., Lorenz, R., Lunine, J., Wall, S., Boubin, G., Reffet, E., Kirk, R., Lopes, R., Stofan, E., Soderblom, L., Allison, M., Janssen, M., Paillou, P., Callahan, P., Spencer, C., the Cassini Radar Team, 2008. Dunes on titan from cassini radar. Icarus 194, 690 – 703.

Reffet, E., Courrech du Pont, S., Hersen, P., Douady, S., 2010. Formation and stability of transverse and longitudinal sand dunes. Geology 38, 491–494.

Rodriguez, S., Garcia, A., Lucas, A., Appéré, T., Gall, A. L., Reffet, E., Corre, L. L., Mouélic, S. L., Cornet, T., du Pont, S. C., Narteau, C., Bourgeois, O., Radebaugh, J., Arnold, K., Barnes, J., Stephan, K., Jaumann, R., Sotin, C., Brown, R., Lorenz, R., Turtle, E., 2014. Global mapping and characterization of titan's dune fields with cassini: Correlation between RADAR and VIMS observations. Icarus 230, 168 – 179.

Rubin, D., Hunter, R., 1987. Bedform alignment in directionally varying flows. Science 237, 276 – 278.

Savage, C. J., Radebaugh, J., Christiansen, E. H., Lorenz, R. D., 2014. Implications of dune pattern analysis for titan's surface history. Icarus 230, 180 – 190.

Sobol', I., 1993. Sensitivity analysis for non-linear mathematical models. Mathematical Modeling & Computational Experiment 1, 407–414.

Soderblom, L., Kirk, R., Lunine, J., Anderson, J., Baines, K., Barnes, J., Barrett, J., Brown, R., Buratti, B., Clark, R., Cruikshank, D., Elachi, C., Janssen, M., Jaumann, R., Karkoschka, E., Mouélic, S., Lopes, R., Lorenz, R., McCord, T., Nicholson, P., Radebaugh, J., Rizk, B., Sotin, C., Stofan, E., Sucharski, T., Tomasko, M., Wall, S., 2007. Correlations between cassini vims spectra and radar sar images: Implications for titan's surface composition and the character of the huygens probe landing site. Planetary and Space Science 55 (13), 2025–2036.

Tokano, T., 2010. Relevance of fast westerlies at equinox for the eastward elongation of titan's dunes. Aeolian Research 2 (2-3), 113–127.

Turtle, E. P., Del Genio, A. D., Barbara, J. M., Perry, J. E., Schaller, E. L., McEwen, A. S., West, R. A., Ray, T. L., 2011a. Seasonal changes in titan's meteorology. Geophysical Research Letters 38 (3).

Ulaby, F. T., Moore, R. K., Fung, A. K., 1982. Microwave remote sensing. Addison-Wesley-Longman, Reading, Mass.

Zribi, M., Ciarletti, V., Taconet, O., 2000. Validation of a rough surface model based on fractional brownian geometry with sirc and erasme radar data over orgeval site. Remote Sensing of Environment 73, 65–72.

Zribi, M., Dechambre, M., 2002. A new empirical model to retrieve soil moisture and roughness from c-band radar data. Remote Sensing of Environment 84, 42–52.

Zribi, M., Taconet, O., Hégarat-Mascle, S. L., Vidal-Madjar, D., Emblanch, C., Loumagne, C., Normand, M., 1997. Backscattering behavior and simulation

comparison over bare soils using sirc/xsar and erasme 1994 data over orgeval. Remote Sensing of Environment 59, 256–266.